applied optics

Influence of aberrations on confocal-based remote refractive index measurements

Helen D. Ford, Daniel Francis, Jonathan M. Hallam, and Ralph P. Tatam*

Engineering Photonics, Cranfield University, Bedford, MK43 0AL, UK
**Corresponding author: r.p.tatam@cranfield.ac.uk*

Received 23 April 2019; revised 15 July 2019; accepted 15 July 2019; posted 15 July 2019 (Doc. ID 365909); published 13 August 2019

Confocal scanning combined with low-coherence interferometry is used to provide remote refractive index and thickness measurements of transparent materials. The influence of lens aberrations in the confocal measurement is assessed through ray-trace modeling of the axial point-spread functions generated using optical configurations comprised of paired aspherics and paired achromats. Off-axis parabolic mirrors are suggested as an alternative to lenses and are shown to exhibit much more symmetric profiles provided the system numerical aperture is not too high. The modeled results compare favorably with experimental data generated using an optical instrument comprised of a broadband source and line-scan spectrometer. Refractive index and thickness measurements are made with each configuration with most mirror pairings offering better than twice the repeatability and accuracy of either lens pairing.

https://doi.org/10.1364/AO.58.006474

1. INTRODUCTION

Low-coherence interferometry is a well-established technique that can be used for measurement of the distance between partially reflective interfaces [1]. It has become particularly prominent since its combination with scanning optics in the form of optical coherence tomography [2], which allows measurements to be made in a plane or even in a volume. The distance that is measured is the optical distance and is dependent on the group refractive index n_g of the medium. Measurement of n_g has been demonstrated using low-coherence interferometry [3] and optical coherence tomography [4]. If the phase refractive index n_p is also desired, however, additional measurements are required. One technique that has frequently been used in combination with low-coherence interferometry is confocal scanning. One of the early reports of this combination [5] demonstrated good measurement of n_p and the physical thickness t of a series of microscope slides but did not measure n_g.

Several solutions have been reported to allow measurement of both n_p and n_g. One involves placing the sample in a special holder with well-defined interfaces [6–8]. Whilst accurate measurement of n_p, n_g, and t was demonstrated, the plate holder, whose interfaces need to be independently calibrated and scanned in addition to the sample, increases the complexity of the alignment and the potential for measurement error. An alternative solution involves an additional measurement of the sample's dispersion made by making the confocal measurement at multiple wavelengths. This has been demonstrated either by using multiple sources [9] or by using spectrometric detection [10]. Spectrometric detection simplifies the optical system and provides a dispersion measurement that is generally higher resolution and closer to the wavelength of interest than using multiple sources. The variation in the confocal distance over the limited bandwidth of the spectrometer is often small though, typically around a micron. This means that errors in the confocal measurement that are larger than this can obscure the gradient of the data from which the dispersion measurement is obtained. Accurate confocal measurement is dependent on accurate localization of the peak observed in the reflected signal as the focus is scanned. The shape of this peak is influenced by the optics used to collimate and focus the beam.

In this paper, we investigate the influence of the optics used in the confocal measurement. Zemax ray-tracing software is used to model the expected confocal peak generated as a planar object is scanned through the focus. Lens aberrations generate asymmetrical broadening, which introduces uncertainty in the determination of the confocal parameter required for refractive index measurement. The use of off-axis parabolic mirrors in the place of lenses eliminates the asymmetry for the front peak; however, spherical aberration introduced by the sample itself causes asymmetry of the rear peak. This effect is particularly evident when using configurations with a high numerical aperture (NA). This problem is well documented in confocal microscopy, which tends to use even higher NA optics than those discussed here [11–13]. The amount of degradation of

the point-spread function (PSF) due to aberration induced at a refractive index interface is dependent not only on the NA of the focusing optics but also on the refractive index and the depth within the aberrating medium [14,15]. Thickness and refractive index data calculated from measurements of the distortion of the PSF have been used to correct for the aberration by introducing a spatial light modulator into the optical system [16].

The results of the ray-trace model presented are compared to experimental results generated using an optical system comprising a broadband source and a line-scan spectrometer. A BK7 window is used as a test object and a range of lens and parabolic mirror configurations are investigated. Asymmetry is observed in the confocal peaks generated using both of the lens systems tested, and in the rear peak of the higher NA mirror configurations, with more symmetric peaks observed with the lower NA mirror systems. This is shown to translate into more consistent refractive index measurements, with the all mirror configurations with an NA below 0.2 offering significantly improved accuracy and repeatability over that of either lens configuration.

2. DESCRIPTION OF THE REFRACTIVE INDEX MEASUREMENT PRINCIPLE

This section briefly describes the refractive index measurement procedure. For a more detailed explanation please see, for example, [9] or [10]. The confocal measurement involves linearly scanning the object through a focused beam so that each of its interfaces is sequentially coincident with the focal point. The reflected light is detected, and the signal observed for a window with two interfaces is a pair of peaks. The separation of the peaks is a quantity Δz that is related to n_p. The expected refraction for a single set of rays impinging on the surface at the angle corresponding to the NA of the beam, i.e., at the radius where the power is $1/e^2$ of the on-axis value, is shown in Fig. 1.

Snell's Law states that, for a sample of refractive index n_p in air, $n_{\text{air}} \sin\theta_1 = n_{\text{air}} \sin\theta_2$. Assuming $\text{NA} = n_{\text{air}} \sin\theta_1$ and performing the trigonometric analysis for the rays shown results in

$$\Delta z = t \times \frac{\sqrt{n_{\text{air}}^2 - \text{NA}^2}}{\sqrt{n_p^2 - \text{NA}^2}}, \tag{1}$$

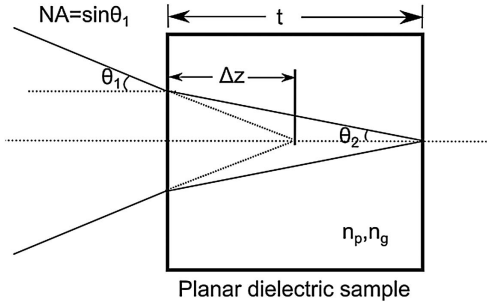

Fig. 1. Refraction by a planar sample of thickness t; rays at angle θ_1, where $\text{NA} = \sin\theta_1$ are refocused from distance Δz inside the front surface onto the rear surface at t. θ_2 is the refracted angle, and n_p and n_g are the phase and group refractive indices, respectively.

where t is the physical separation of the interfaces. Equation (1) is valid for all NA; however, for paraxial rays and small values of NA, this is well approximated by the much simpler expression $\Delta z = t/n_p$. The implicit assumption, when Eq. (1) is used by other authors for determination of the confocal distance Δz, is that the value of Δz thus obtained corresponds to the maximum of the axial point-spread function for confocal distance measurements within a planar dielectric sample. This theory is valid for all surfaces with a flatness equal to or better than the wavelength of the source.

The low-coherence measurement involves bringing the object beam to focus on each interface in turn and scanning a reference mirror in the other arm of an interferometer so that it passes through the point of phase matching. For a window with two interfaces, a pair of interferometric fringe patterns are seen whose width is determined by the coherence length of the source. The separation of the fringe envelopes Δl is a quantity related to n_g by

$$\Delta l = t \times n_g. \tag{2}$$

Equations (1) and (2) can be combined using the expression for chromatic dispersion

$$n_g(\nu) = n_p(\nu) + \nu \frac{dn_p(\nu)}{d\nu}, \tag{3}$$

where ν is the optical frequency, to yield [9]

$$t^2 = \frac{\Delta l \Delta z}{1 - \frac{\nu}{\Delta z}\frac{d\Delta z}{d\nu}}. \tag{4}$$

The expression is therefore dependent on a dispersion term $d\Delta z/d\nu$, which can be obtained by making the confocal measurement at multiple wavelengths. Equation (4) is derived assuming a small numerical aperture. For numerical apertures that are large enough to invalidate the assumption, the solution can be obtained using a polynomial expansion [9,10]. Once t has been determined from the measurement data, the refractive index components are readily obtained from Eqs. (1) and (2).

3. RAY-TRACE ANALYSIS OF OPTICAL CONFIGURATIONS FOR CONFOCAL METROLOGY

The optical complexity of the confocal metrology system is low, comprising a collimation element followed by a focusing element. Ideally, to avoid power loss, the collimator NA is selected to exceed the typical 0.10–0.15 NA of the delivery optical fiber. The NA onto the sample is controlled via the ratio of the focusing element focal length to that of the collimator, with the width of the detected axial intensity PSF reducing as the NA onto the sample is increased. A higher NA is often more appropriate for thinner samples to ensure separation of the profiles for the front and back sample surfaces.

In an experimental system, the shape and width of the peak PSF around the focus is affected by aberrations of the beam delivery system. Typically, achromats or multi-element microscope objectives, are used for collimation and focusing of the super-luminescent diode (SLD) source. These are "well-corrected" lenses, the phrase usually implying that the actual beam spot radius at the focus is smaller than that obtained using

Gaussian beam theory. In imaging applications, beam-waist radius at the focus is the most important parameter. However, in the current application, we are interested not only in the beam profile at best focus but also in the axial PSF as a sample surface is tracked through the focus.

The axial PSF is investigated here for pairs of either aspheres or achromats. Microscope objectives, where optical data for constituent lenses is not usually provided by the manufacturer, have not been considered. Systems have been modeled using optical elements from Thorlabs, Inc. since material data and element dimensions are available online for these components, allowing a Zemax model to be readily created. Elements used in each system are listed in Table 1. A monochromatic 1 W source of wavelength 1000 nm is assumed and the sample is, in each case, a BK7 plate of 1 mm thickness. The monochromatic source is appropriate for our experimental system, which uses spectrometer detection, because the resolution of the spectrometer means that light is effectively monochromatic at each pixel bin. The input NA is constant, to the second decimal place, at a value of 0.11 across all modeled systems, and NA values onto the sample are maintained within a range that allows results to be readily compared. Experimentally, the intensity measured is not simply the on-axis value but requires integration over the area of the confocal aperture, in this case the core of the optical fiber used to deliver light to the sample and to collect reflected power. The fiber core has been assumed to have a radius, commensurate with the input NA of the system, of 3 μm.

Zemax ray-tracing takes no account of the diffraction that affects beam profiles close to the focus. Gaussian beam theory gives the axial evolution of the detected intensity as

$$I(z) = I_0(1 - \exp(-2r^2/\omega^2(z)), \tag{5}$$

where the beam waist ω as a function of distance along the optical axis z is

$$\omega(z) = \omega_0\sqrt{1 + (z/z_R)^2}, \tag{6}$$

where z_R is the Rayleigh range.

Strictly, Gaussian beam theory is not appropriate for the analysis of aberrated beams because aberration causes the beam profile to deviate from a Gaussian form. However, at lower NA when aberration is small, significant diffraction broadening of the beam profiles is expected, with the Gaussian beam-waist radius and Rayleigh range offering a good approximation to radial and axial intensity profiles under these conditions. At higher NA, diffraction broadening is reduced and the shape of the axial PSF will be dominated by aberration effects. The greatest uncertainty over beam profile shape is experienced in the overlap regime, where diffraction and aberration make contributions of comparable magnitude to the beam-spot broadening. Here, we present the symmetrical, diffraction-broadened profiles, derived from Gaussian beam theory, overlaid on the computational ray-tracing curves. It is not altogether obvious what the correct relative positioning of the two sets of data should be. We have positioned the diffraction-broadened peak for the front sample surface at the paraxial focus length (obtained by running the Zemax model with a very small NA value) and the peak for the rear surface at the NA-appropriate beam focus predicted by Eq. (1) above. Thus, the diffraction-broadened peaks represent the outcome that would be expected for an unaberrated input beam, using the theory of Kim *et al.* [9].

A. Collimation and Focusing Optic Pairs

Zemax ray-tracing has been used to model the behavior of the confocal system with light emerging from the delivery fiber treated as a Gaussian point source and different types of optical elements employed for collimation and focusing. We consider the following optical arrangements: (i) paired aspherics, (ii) paired achromats, and (iii) paired parabolic mirrors, as shown in Fig. 2. The NA onto the planar sample can be adjusted by changing the focal length ratio between the collimation and focusing optics.

Results of the Zemax model for paired aspherics and paired achromats are shown in Fig. 3. In these plots, the right-hand peak of each pair results from the front sample surface and the left-hand peak from the rear surface. Features to note include the width and shape of the peaks and the separation distance between peak pairs. It is immediately clear, comparing the red peaks from Zemax modeling with the gray peaks representing diffraction broadening, that lens aberration causes additional broadening and asymmetry of the axial intensity profiles. The asymmetry is easier to observe in the low NA plots. At higher NA, additional distortions of the profile can occur, as seen for the achromat pair in Fig. 3(d), where a small, sharp side-lobe occurs to the left of each main peak. This is believed

Table 1. Summary of the Different Lens and Off-Axis Parabolic Mirror Configurations Used in the Assessment[a]

System Name	Collimator	f/mm	Input NA	Focusing Element	f/mm	Sample NA
As1	C560TME-B	13.9	0.107	A240TM-B	8.0	0.185
As2	C560TME-B	13.9	0.107	C560TME-B	13.9	0.107
As3	C560TME-B	13.9	0.107	C280TMD-B	18.4	0.080
Ac1	AC127-025-B	25.0	0.110	AC080-016-B	16.0	0.172
Ac2	AC127-025-B	25.0	0.110	AC127-025-B	25.0	0.110
Ac3	AC127-025-B	25.0	0.110	AC254-035-B	35.0	0.079
OAP1	MPD019	25.4	0.106	N/A	10.0	0.269
OAP2	MPD019	25.4	0.106	N/A	12.7	0.212
OAP3	MPD019	25.4	0.106	MPD00M9	15.0	0.179
OAP4	MPD019	25.4	0.106	MPD019	25.4	0.106
OAP5	MPD019	25.4	0.106	MPD01M9	33.0	0.082

[a]As1-3 are the asphere pairs, Ac1-3 are the achromat pairs, and OAP1-5 are the parabolic mirror pairs. The serial numbers for each element are from the Thorlabs library.

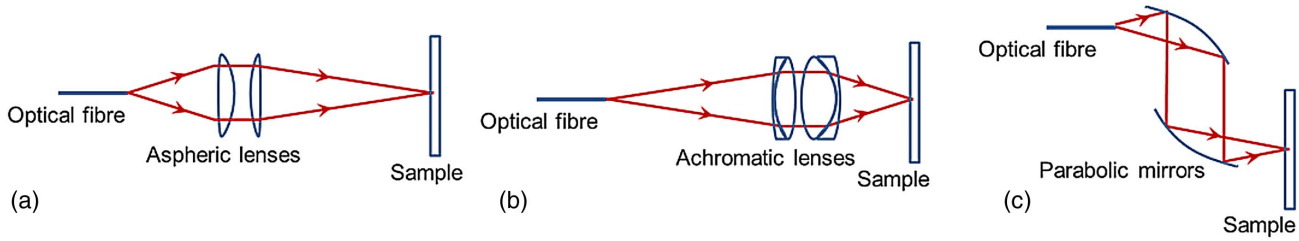

Fig. 2. Focusing arrangements showing (a) aspheric lens pair with NA reduction, (b) achromat lens pair with NA increase, and (c) off-axis parabolic mirror pair with no NA change.

to be due to the aberration present in these optical elements. Conversely, at lower NA, a problem can occur as demonstrated by the asphere pair in Fig. 3(c). Here the peaks are not well separated, showing that the NA is too low for this sample thickness and lens type.

Poor separation of the peaks implies that light is returned simultaneously from both sample surfaces and is undesirable for two reasons. First spectroscopic detection, as used in our system, results in a typical coherence length of several millimeters, which means that unwanted fringing can occur, caused by self-interference between reflections from the front and rear sample surfaces. Even in systems where the output is collected on a single detector and integration over all wavelengths eliminates fringing, the overlap of each peak wing with the neighboring maximum can still cause "peak-pulling," resulting in small inward shifts of the peak maxima and a measured Δz lower than the correct value.

In each pair of intensity profiles, the shape is similar for both front and rear surfaces, indicating that lens aberration is the dominant contributor to broadening. Asymmetry, both for aspheres and achromats, is pronounced. The intensity falls away rapidly to the left of the maxima, which suggests possible problems in identifying peak positions; although diffraction broadening will slightly soften the sharp drop-off of intensity, the precise positions of these maxima are likely to be very sensitive to small variations in experimental geometry.

It is clear also that the aberration causes a shift in the apparent peak positions compared with paraxial values. This is

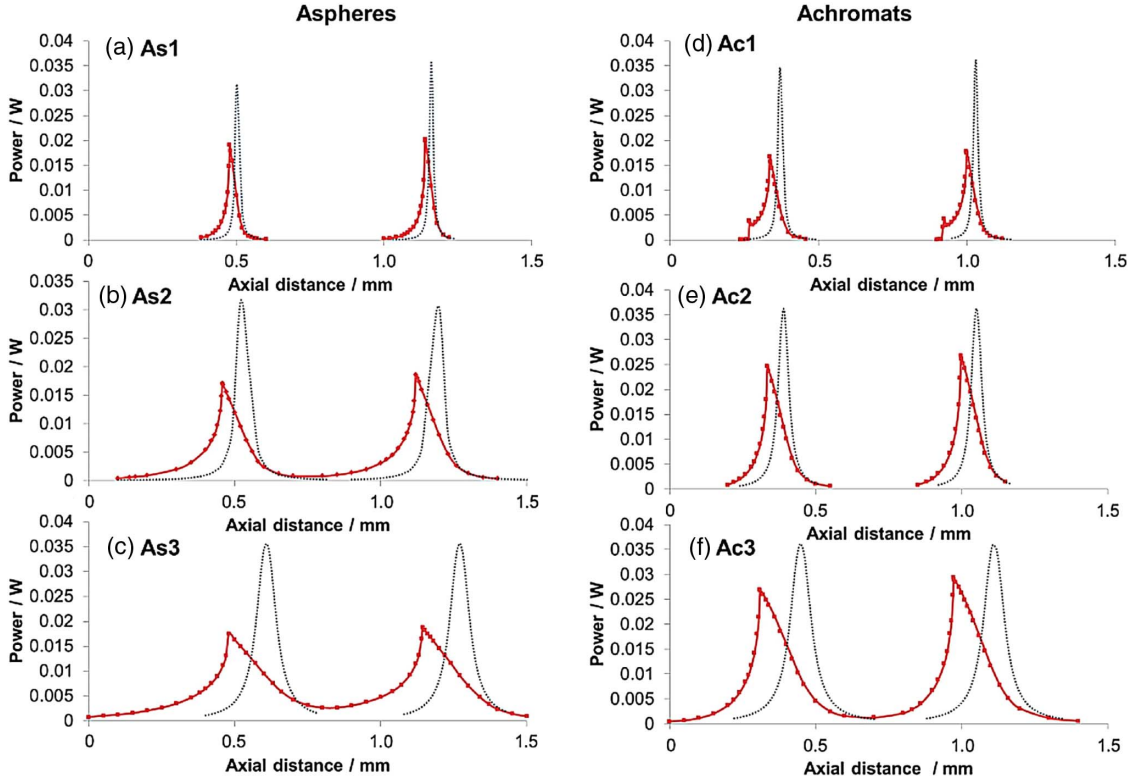

Fig. 3. Axial PSFs through the focus from the Zemax model (red curves), and with Gaussian broadening only (gray curves), for a beam focused by (a)–(c) paired aspheres or (d)–(f) paired achromats, onto a 1 mm thick planar sample, such that the focus coincides with the front (right-hand peaks) or rear (left-hand peaks) surface. Lens combinations correspond to system names given in Table 1. The NA at sample is (a) 0.185, (b) 0.107, (c) 0.080, (d) 0.172, (e) 0.110, and (f) 0.079.

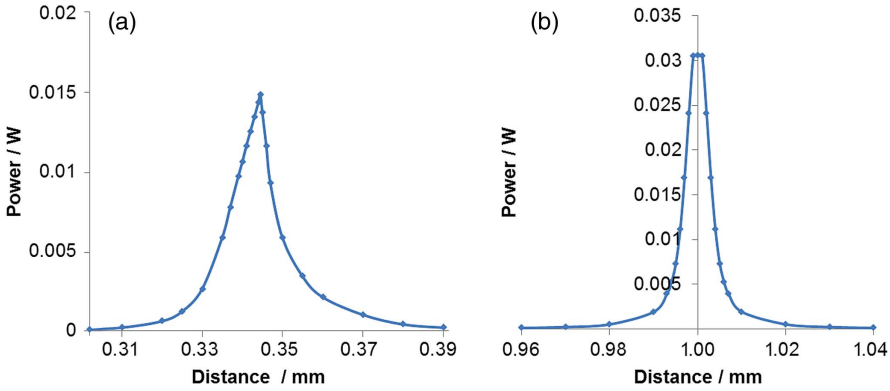

Fig. 4. Axial PSFs through the focus from the Zemax model for a beam focused by paired paraboloidal mirrors onto a 1 mm thick planar dielectric sample. Curves correspond to the focus on (a) rear and (b) front sample surfaces, with an NA of 0.212 at the sample.

acceptable provided that the offset is identical for both front and rear sample surfaces. However, problems are anticipated at higher NA because of the spherical aberration introduced by the front sample surface. Refraction, as shown in Fig. 1, occurs at the dielectric interface for all incident rays, not just those at the angle for which NA is defined. Equation (1), with the sine of each ray angle substituted for NA, defines how Δz varies for all rays within the convergent incident beam. Paraxial rays are focused closer to the front sample surface than marginal rays. For a convergent Gaussian beam, 86.5% of the beam power resides, by definition, in rays with incident angles smaller than that corresponding to the beam NA.

The aberrating effect of the sample surface can be studied in isolation by replacing the collimating and focusing lenses in the Zemax model with off-axis parabolic (OAP) mirrors. The incident beam is then unaberrated in air, i.e., will produce, in the ray model, a perfect focus with all rays converging to an infinitely small beam spot. Figure 4 shows a pair of axial intensity profiles from the OAP mirror model for a focus NA of 0.212 and a 1 mm thick BK7 sample with a refractive index of 1.5074. It is immediately clear that the axial intensity profile observed for light reflected from the rear sample surface is asymmetrically broadened, as a result of spherical aberration from the front surface, though the asymmetry is much less than that introduced by the lenses. In contrast, the intensity profile for the front-surface reflection is perfectly symmetrical and considerably narrower. The slight flattening at the top of this peak occurs because Zemax does not account for the Gaussian beam diffraction close to the focus.

The confocal distance Δz is calculated as the difference between the positions of the two peaks in each pair. For asymmetrical peaks, consideration must be given to the criterion used to define the peak position. We have selected two methods for comparison: (a) axial position corresponding to the intensity maximum and (b) axial position corresponding to the centroid of the upper two-thirds of the peak profile. The different methods yield slightly different position values. This becomes important when, as here, distance measurements are required with an accuracy and precision of better than 1 μm. Our confocal metrology measurement uses axial peak position as a proxy for the physical position of sample surfaces. Since thickness only is required, an offset between the two parameters can be tolerated provided, crucially, that it is the same for all surfaces in a given sample.

For the peak pair shown in Fig. 4, the paraxial approximation gives the distance of the rear sample surface relative to the front surface as 0.6634 mm. Using Eq. (1), the same distance is calculated to be 0.6548 mm. The maximum of the modeled intensity profile occurs at a distance of 0.6555 mm and the centroid at 0.6576 mm. Although Eq. (1) is preferable for nonparaxial imaging, a discrepancy still exists between the expected peak position and the actual peak position. The OAP mirror model was repeated for different values of incident beam NA, as detailed in Table 1. The model has been used to measure Δz for a range of NA values, using the two methods identified above to extract the peak position for the reflection from the rear sample surface. Examples of the resulting peak pairs are shown in Fig. 5.

An error value can be obtained as the difference between the Δz value from the model, and that calculated using Eq. (1), for each NA. Error values are plotted in Fig. 6 using peak locations either calculated from the centroid of the top two-thirds of each peak (a) or by simply taking the peak maxima (b). Figures obtained using the maximum value criterion are slightly lower than those obtained from centroiding. For both methods, the difference from the predicted value is small below an NA of about 0.2 but starts to rise rapidly for NA values above this, with the calculated Δz being an underestimate of that expected experimentally. We attribute this to averaging of the focus distance over all rays within the incident beam, most of which have smaller incident angles than the particular rays, shown in Fig. 1, that define the focus NA. From Fig. 6, it appears that significant errors in measured sample thickness and refractive index might be expected at higher NA, when Eq. (1) is used to extract these parameters from measured Δz values. However, the error is partially compensated by the practice of back-calculating system NA from measurements on a calibration sample of known thickness and refractive index. This is acceptable provided that the refractive index of subsequently measured samples does not differ excessively from the refractive index at which NA is determined.

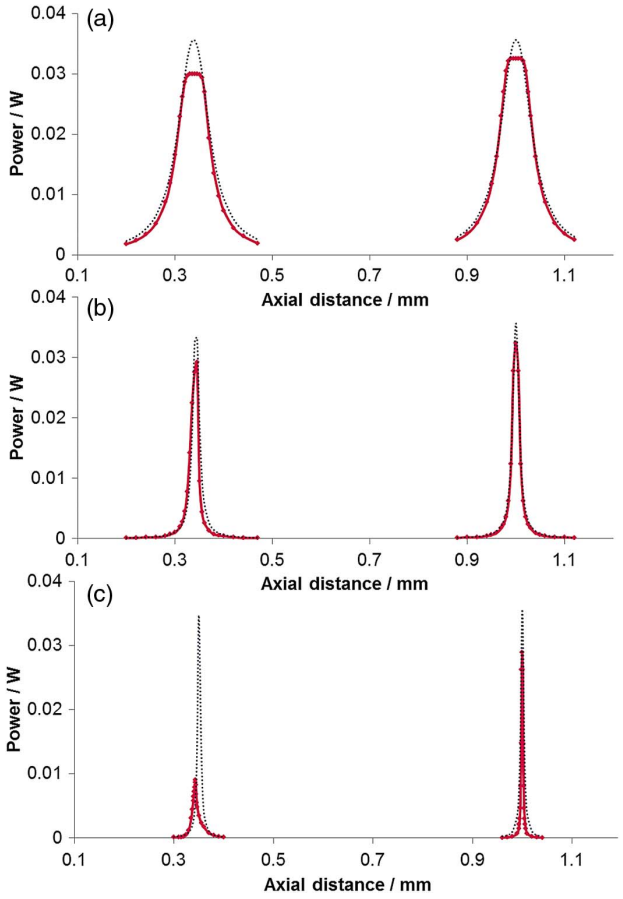

Fig. 5. Axial PSFs through the focus from the Zemax model (red curves), and with Gaussian broadening only (gray curves), for a beam focused by off-axis parabolic mirrors onto the front (right-hand peaks) or rear (left-hand peaks) surface of a 1 mm thick planar sample. Focusing system details are given in Table 1; (a) OAP5, NA at sample 0.082; (b) OAP3, NA at sample 0.179; and (c) OAP1, NA at sample 0.269.

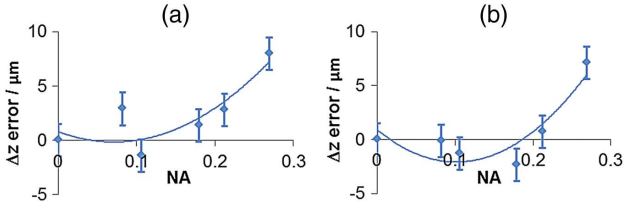

Fig. 6. Difference between Δz values from Zemax model and those calculated using Eq. (1), as a function of NA, using peak positions defined as (a) centroid (with threshold at 33% of peak maximum) and (b) maximum value.

B. Discussion

While system NA and confocal peak positions are the primary considerations, PSF broadening is also of concern because peak overlap is undesirable. For a Gaussian beam, the Rayleigh range gives an indication of the distance over which good focus is obtained. At 1000 nm wavelength, an NA of 0.04 results in a Rayleigh range of about 200 μm. However, in lens-based focusing systems, aberrations broaden the peaks and increase the NA required for full separation. If reasonable care has been taken to ensure good on-axis alignment of the system optics, measurement error is dominated by lens aberrations. For aspheres, Fig. 3 suggests that a minimum NA of about 0.1 is necessary to ensure full peak separation for a 1 mm thick sample and for achromats a minimum NA of about 0.08. For thinner samples, much higher NAs become necessary. Since peak width is inversely proportional to the square of the NA, an NA above 0.3 will be required to make measurements on a 100 μm thick sample, significantly increasing peak distortion and calculation-related errors.

Lenses, of course, suffer also from chromatic aberration. The dispersion of the sample itself is accounted for in the calculations but not chromatic aberration of the focusing lenses. For lenses with focal lengths of a few tens of millimeters, focal shifts up to a few tens of a micron are typical over a 100 nm wavelength range at 1000 nm center wavelength, with the shift for an asphere being typically two to three times worse than that for an equivalent achromat. The focal shift is very large compared with sample dispersion; its effect can be seen in sets of peak pairs from any given sample, which appear shifted relative to one another as the wavelength changes along the spectrometer array. However, NA change is the main driver of spherical aberration and peak shape variation. The wavelength variation has an insignificant effect on system NA, and the form of the axial PSF is essentially invariant with wavelength. Hence, in this application, where only relative distances between front and rear sample surfaces are required, chromatic aberration does not matter, although we note that a further effect of the use of parabolic mirrors for beam focusing will be to eliminate the focal shift seen in the current lens-based systems.

4. EXPERIMENTAL VALIDATION

A. Description of Experimental System

A schematic of the system is shown in Fig. 7. The source was a SLD with a center wavelength of 840 nm, a bandwidth of 50 nm, and an optical power of 10 mW. The SLD is part of a Superlum M-T-850-HP-I Broadlighter system. An interferometer is formed using a broadband fiber-optic coupler (Thorlabs TW850R2A2), which has a bandwidth of 850 ± 100 nm and a 90:10 split ratio. The fiber core acts as the confocal aperture and has a diameter of 4.4 μm, which provides a system input NA of 0.13. Physik Instrumente V408 linear translation stages were used to mount the sample in the confocal channel and a reference mirror and focusing lens in the reference channel. They provide a travel range of 50 mm, a maximum velocity of 500 mm/s, and a minimum incremental motion of 20 nm. Light on the return port of the coupler was directed to a spectrometer (Bayspec OCT spectrograph @850), which has an approximate bandwidth of 50 nm. The spectrometer incorporates a line-scan camera (Basler spL4096-140 km), which has an array size of 4096 pixels and a maximum acquisition rate of 140 kHz with 12-bit digital resolution. The camera was interfaced to a computer using a National Instruments PCIe-1433 frame grabber.

Measurements were made with a range of optical configurations in the confocal channel conforming to those used in the

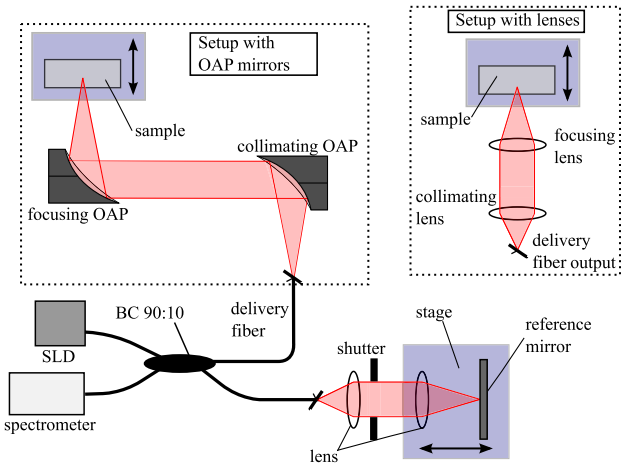

Fig. 7. Schematic showing the configuration of the experimental system. SLD is the super-luminescent diode, BC is the broadband coupler, and OAP is the off-axis parabolic mirror. The blue shading indicates which components are mounted on the translation stages. The inset shows the configuration used when confocal measurements are made with lenses.

ray-tracing assessment described in the previous section. These included a range of paired OAP mirrors with different system NAs, a pair of achromatic lenses, and a pair of aspheric lenses. The schematic in Fig. 7 shows the system set up using OAP mirrors, with the lens setup shown in the inset. The confocal measurements were made by scanning the object linearly through the focus of the beam and recording the intensity integrated over the full spectrometer array. The object used was a BK7 window (Edmund Optics) with a nominal thickness of 3 mm and flatness of $\lambda/4$. The reference arm is not needed for the confocal measurements; therefore, this beam is blocked using a shutter.

Alignment of off-axis parabolic mirrors can be challenging, and particular care needs to be given to the orientation of the mirror [17]. The flat side of the mirror mount should be oriented orthogonally to the incoming beam. If the mirror is oriented the other way, with the flat of the mount opposite to the incoming beam, then a collimated beam will not be produced and a significant amount of coma will be introduced, as shown in Fig. 8(a). To ensure accurate collimation it is helpful to use a shear plate interferometer placed in the beam path. Since the coherence length of our source is much shorter than the shear plate separation, the SLD was replaced with an 830 nm laser diode (SDL-5431-G1) for the purposes of alignment. A CMOS camera (Baumer HXC-13) placed after the shear plate was used to monitor the fringe pattern. The OAP was adjusted until parallel straight-line fringes were observed oriented parallel to an alignment notch etched into the diffuse screen of the shear plate, as shown in Fig. 8(b).

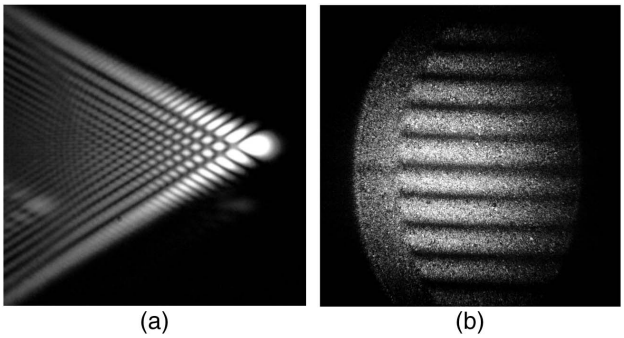

Fig. 8. Image of the beam profile recorded with the collimating OAP mirror in the incorrect orientation shows significant coma in part (a). When correctly oriented and collimated, the beam profile through a shear plate interferometer shows straight line fringes oriented parallel to an alignment groove etched into the diffuse screen of the interferometer in part (b).

B. Confocal Peak Shapes with Different Optical Configurations

The achromatic lens pairing was a Thorlabs AC080-020-B-ML with 20 mm focal length used to collimate and an AC080-016-B-ML with 16 mm focal length used to focus. The aspheric lenses used were a pair of Newport 5725-B-H lenses with 11 mm focal length. Each of the lenses was antireflection coated with an effective range covering 650–1050 nm. Confocal peaks obtained with the lens-based configurations are shown in Fig. 9. The peaks obtained with the achromats are shown in Figs. 9(a) and 9(b) and the peaks obtained with aspheres shown in Figs. 9(c) and 9(d). The peaks reflected from the rear surface are shown on the left [Figs. 9(a) and 9(c)] and from the front surface on the right [Figs. 9(b) and 9(d)]. The confocal peaks are a measure of the axial point-spread function (APSF) of the optical system used to bring the beam to focus. The functional form of the APSF has been studied in the case of OCT in scattering and nonscattering media [18]. This study used Gaussian beam theory based on single-mode fiber optic delivery to derive a more simplified expression for the APSF than those previously reported. The expression for the APSF, h, in the nonscattering case is given by [18]

$$h(d) = \frac{1}{\left(\frac{d}{z}\right)^2 + 1}, \tag{7}$$

where d is the focal shift and

$$z = \frac{\pi n_p \omega}{\lambda}, \tag{8}$$

where ω is the beam waist.

The thin black curves in Fig. 9 are the nonlinear least squares fits to the APSF computed using the trust-region-reflective algorithm [19]. These curves represent the aberration-free case for each optical system and serve to illustrate the asymmetry introduced by the aberrations present. The data in Fig. 9 shows that, whilst not having quite such extreme asymmetry as some of the modeled results shown in Fig. 3, there is still a significant diversion from the APSF fit. Also, the side peak predicted in the higher NA achromat model [Fig. 3(d)] is clearly visible to the left of the main peak in Figs. 9(a) and 9(b). Whilst the peaks are asymmetric, they are not necessarily broader than the expected curve, suggesting that the lenses are better corrected than is suggested by the ray-trace model.

The OAP mirrors that were used were from the Thorlabs MP range and the reflective material of each is protected gold.

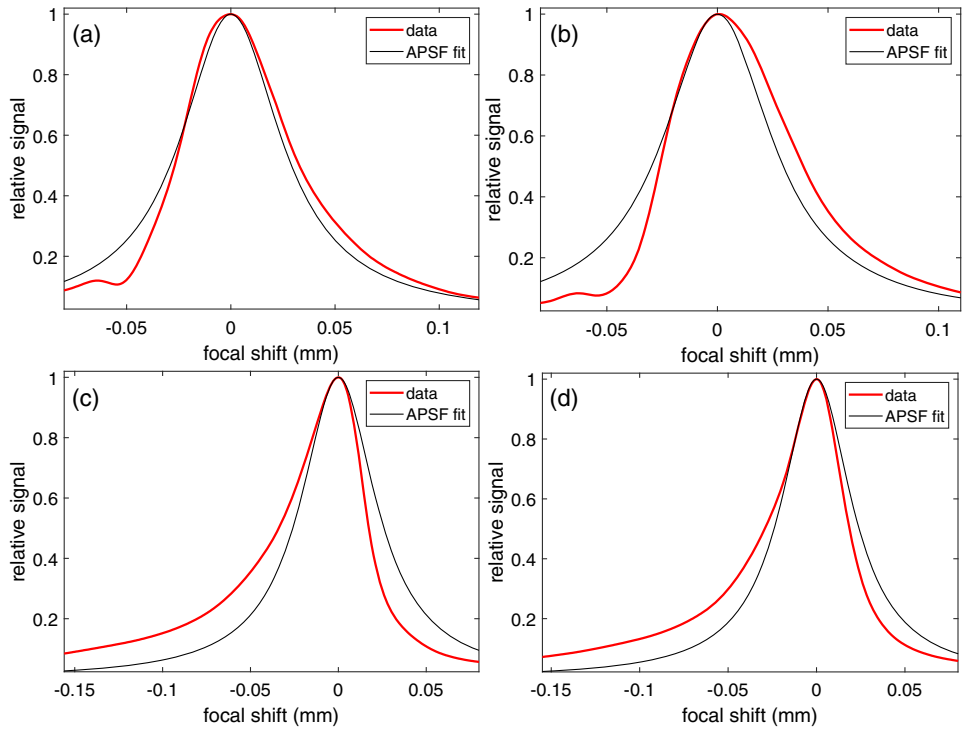

Fig. 9. Experimentally obtained confocal peaks (thick red curves) with the fit to the APSF given in Eq. (7) (thin black curves). The peaks shown were obtained using paired achromats [(a) rear peak and (b) front peak] and using paired aspheres [(c) rear peak and (d) front peak]. The NA at the sample is 0.150 for the achromats and 0.121 for aspheres.

Each of the measurements was made using a mirror with a focal length of 25.4 mm to collimate the beam. The focusing optics used had focal lengths of 15 mm, 25.4 mm, 33 mm, and 50.8 mm. The first three of these combinations correspond to OAP systems 3–5 in Table 1. The confocal peaks obtained with the various OAP mirror configurations are shown in Fig. 10. The rear peaks are shown on the left of the figure [Figs. 10(a), 10(c), 10(e), and 10(g)], and the front peaks are shown on the right [Figs. 10(b), 10(d), 10(f), and 10(h)].

The effect of spherical aberration introduced by the front sample surface is evident in the highest NA configuration, as can be seen in the asymmetry of the peak in Fig. 10(a) relative to Fig. 10(b). This is not readily apparent in the peak shapes of the lower NA configurations, however. The peak width increases with decreasing NA as would be expected. Some of the properties of the peaks in Figs. 9 and 10 are summarized in Table 2. The full width at half-maximum (FWHM) is provided for each of the peak, as is the root-mean-square (rms) error of the fit to the APSF. This serves to provide an indicator of the symmetricity of each of the peaks, with a better fit, i.e., a lower rms error, implying a more symmetric peak. The rms error values correspond to that which is visually apparent, with larger errors observed in each of the peaks obtained with the lens configurations, and in the rear peak obtained with the highest NA mirror configuration. The broadening effect of the aberration is less noticeable here than in the modeled data and only really apparent in the broadening of the rear peak of the highest NA mirror configuration. There is no apparent broadening of the peaks generated with the lenses relative to the mirrors when comparing configurations of a similar NA.

C. Refractive Index Measurements with Different Setups

To determine the sample thickness and refractive index values, three measured quantities are required to satisfy Eq. (4). These are the confocal term Δz, the low-coherence term Δl, and the dispersion term $d\Delta z/d\nu$. Δz is obtained by scanning the sample stage through the focus and measuring the separation of the peaks reflected from each surface. The low-coherence measurement is made by placing the sample so that the focus is at each surface in turn and scanning the reference mirror. When the difference in the path lengths of the two interferometer arms is within the coherence length of the source, a burst of fringes is observed in the integrated signal. Δl is obtained by measuring the separation of the peak of the fringe envelopes associated with the two surfaces. The fringe envelope is calculated from the magnitude of the analytic signal, which can be determined using the Hilbert transform [20,21].

Fringe envelopes obtained from the front surface of the sample using the aspheric lens configuration and the OAP mirror configuration with a 25.4 mm focuser are shown in Figs. 11(a) and 11(b), respectively. The fringe bursts acquired with the OAP mirror pairings are broader and of lower modulation than those obtained with either lens pairing for both front and rear surfaces. The dispersion term is calculated by dividing the spectrometer array into a number of equally separated subarrays. The mean signal value is calculated within each subregion, allowing Δz to be calculated at different wavelengths. An example of the variation of Δz with wavelength is shown in Fig. 11(c). $d\Delta z/d\nu$ is then found from the gradient of this data with respect to the optical frequency. The sample thickness and

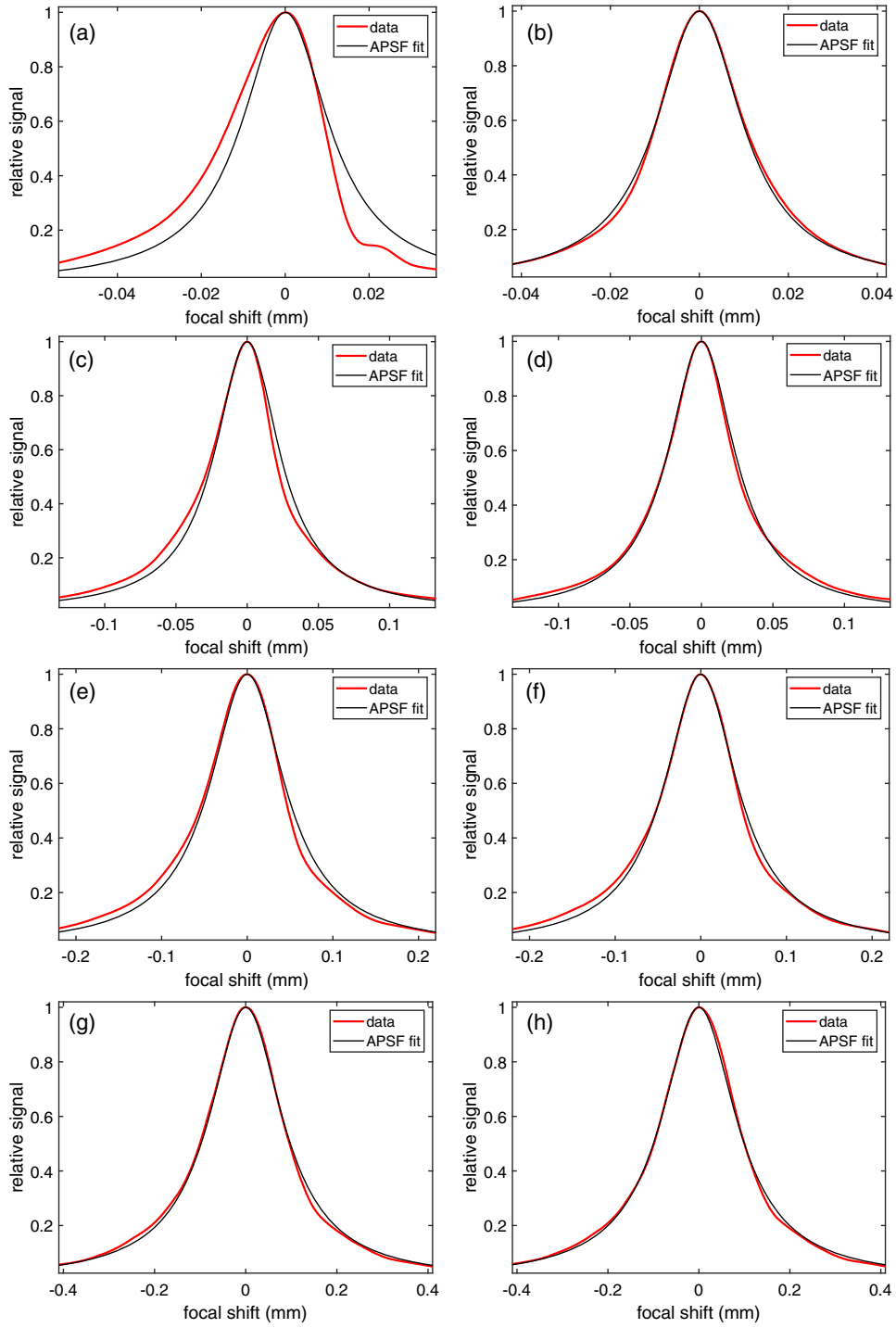

Fig. 10. Experimentally obtained confocal peaks (thick red curves) with the fit to the axial PSF given in Eq. (7) (thin black curves) for different OAP mirror configurations. In each case the collimating optic is the same ($f = 25.4$ mm) with a different focusing optic in each case providing an NA at the sample of (a) and (b) 0.202; (c) and (d) 0.121; (e) and (f) 0.093; and (g) and (h) 0.061. The rear peaks are shown on the left, and the front peaks are shown on the right.

refractive index values are calculated from these terms using Eqs. (1)–(4).

A summary of the thickness and refractive index measurements made with each optical configuration is shown in Table 3. Each measurement was made ten times and the standard deviation of these measurements is given in the table. The percentage error is derived from the difference between the measured value and the reference refractive index values, which for BK7 at 840 nm are 1.5100 for n_p and 1.5252 for n_g [22]. The reference thickness value was obtained by measuring the

Table 2. Summary of the Properties of the Confocal Peaks Obtained with Different Optical Configurations (Shown in Figs. 9 and 10)[a]

Collimator	Focuser	Sample NA	Front FWHM (μm)	Rear FWHM (μm)	rms error (front)	rms error (rear)
Achromat ($f = 20$ mm)	Achromat ($f = 16$ mm)	0.150	64.9	59.8	0.091	0.051
Asphere ($f = 11$ mm)	Asphere ($f = 11$ mm)	0.121	48	51.2	0.080	0.106
OAP mirror ($f = 24.5$ mm)	OAP mirror ($f = 15$ mm)[b]	0.202	23.7	26.6	0.013	0.083
OAP mirror ($f = 24.5$ mm)	OAP mirror ($f = 24.5$ mm)[c]	0.121	55.0	52.6	0.015	0.033
OAP mirror ($f = 24.5$ mm)	OAP mirror ($f = 33$ mm)[d]	0.093	101	104	0.019	0.027
OAP mirror ($f = 24.5$ mm)	OAP mirror ($f = 50.8$ mm)	0.061	196	197	0.011	0.013

[a]The error columns refer to the rms error of the fit to the APSF.
[b]OAP3 in Table 1.
[c]OAP4 in Table 1.
[d]OAP5 in Table 1.

sample thickness using Mitutoyo MDH digital micrometer gauge with 0.1 μm resolution. The thickness of the BK7 window used here was measured to be 3.1230 ± 0.0002 mm.

Each of the OAP mirror configurations shows much better measurement consistency than the lens configurations, with the standard deviation generally being less than half that of the lens configurations. The measurement accuracy is better in most cases as well, although it should be noted that the measurement of n_g and t is very poor for the high-NA mirror configuration. The accuracy generally improves with decreasing NA, with the lowest NA configuration exhibiting the lowest percentage error. This is likely due to the introduction of spherical aberration by the front sample surface, which causes distortion of the rear peak but not the front peak, as we have seen in Figs. 4, 5(c), 10(a), and 10(b). That better performance can be expected from lower NA configurations is greatly beneficial for the

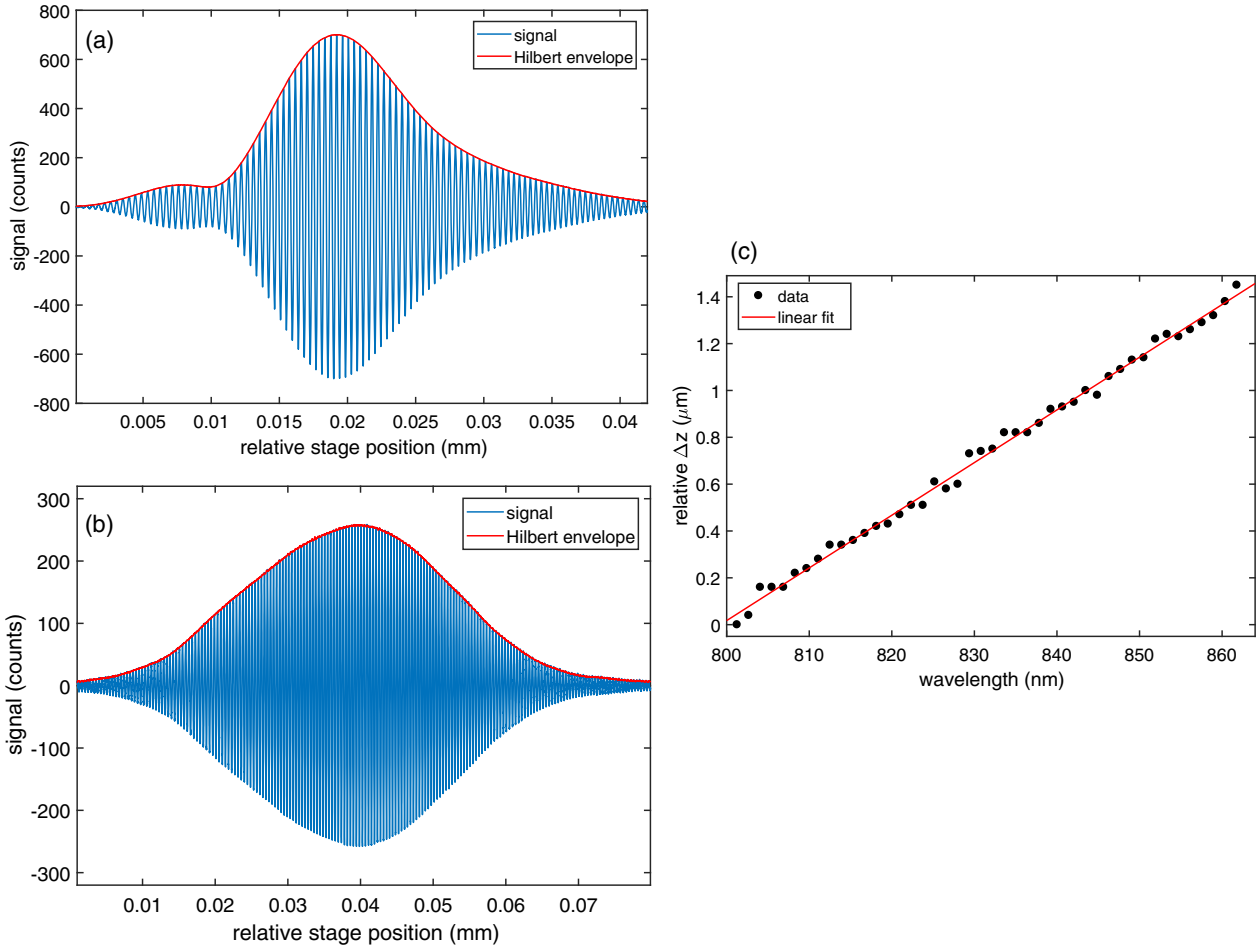

Fig. 11. Low coherence fringe envelopes obtained from the front sample surface using (a) the aspheric lens configuration and (b) the OAP mirror configuration with a 25.4 mm focuser. The variation in the confocal parameter Δz from which the dispersion data $d\Delta z/d\nu$ is acquired (also obtained with OAP pairing with a 25.4 mm focuser).

Table 3. Summary of Thickness and Refractive Index Measurements for a Range of Different Optical Configurations

System	n_p	StDev n_p	Error (%) n_p	n_g	StDev n_g	Error (%) n_g	t	StDev t	Error (%) t
Paired achromats	1.5088	0.0012	0.078	1.5237	0.0013	0.098	3.1277	0.0028	0.118
Paired aspheres	1.5114	0.0026	0.093	1.5244	0.0017	0.056	3.1257	0.0018	0.050
OAP (15 mm focuser)[a]	1.5094	0.0005	0.042	1.5188	0.0004	0.418	3.1382	0.0010	0.450
OAP (25.4 mm focuser)[b]	1.5106	0.0004	0.039	1.5246	0.0005	0.038	3.1264	0.0012	0.072
OAP (33 mm focuser)[c]	1.5093	0.0005	0.044	1.5247	0.0004	0.031	3.1257	0.0010	0.050
OAP (50.8 mm focuser)	1.5103	0.0006	0.022	1.5255	0.0006	0.020	3.1238	0.0012	0.010

[a]OAP3 in Table 1.
[b]OAP4 in Table 1.
[c]OAP5 in Table 1.

development of remote refractive index sensors. This is because the lower the NA at sample, the longer the standoff distance can be and thus allows larger test objects to be measured, provided the individual layer thickness is large enough to provide adequate peak separation.

5. CONCLUSIONS

The ray trace model described in Section 3 illustrated several potential problems that can be caused by lens aberrations in the confocal optics. In particular, distortion of the peak can introduce errors in the peak localization, which results in measurement error in the confocal term Δz and thus inaccuracy in the thickness and refractive index values. This is exacerbated if the level of distortion is different for the front peak than for subsequent peaks as is likely to occur for high-NA configurations due to aberration induced by the sample itself. Another issue is aberration-induced peak broadening, which can limit the thickness of samples that can be measured with a particular configuration.

Replacement of the lenses with parabolic mirrors should significantly reduce input aberration, resulting in much more symmetrical peaks. This will substantially mitigate many of these issues; however, unless corrections are applied the maximum NA will still be limited by the spherical aberration of the sample, as shown in Fig. 6. Beyond an NA of about 0.18, a systematic and increasing offset in Δz would be expected.

The experimental measurements confirm much of what was predicted by the ray trace model. Asymmetry of the confocal PSF occurs for both the front and rear peaks in both of the lens configurations, though not quite to the extent predicted in the model. This is perhaps due to the lenses being better corrected than is suggested by the model. The parabolic mirror configurations do yield more symmetric peaks and this is evidenced by the quality of the fitted data to the APSF for each configuration. This is true of all peaks generated with the mirrors save for the rear peak generated with the highest NA configuration. There is no noticeable narrowing of the peaks when moving from lenses to mirrors, however, as suggested by comparing the measured FWHMs of peaks generated with similar NA configurations. The improved symmetricity of the peaks obtained with the mirror configurations does appear to improve the accuracy and precision of the thickness and refractive index measurements, with lower standard deviation and percentage errors obtained for each mirror configuration save the highest NA one.

For many samples, maintenance of the NA below about 0.18 should minimize problems with sample-induced spherical aberration. In principle, because Δz is linear in t, the fractional distance error introduced by ignoring spherical aberration at the sample is dependent only upon sample refractive index and NA. This could be tabulated for a range of input conditions, allowing correction factors to be obtained that should result in improved thickness and refractive index values for higher NA configurations. This could hence extend the range of values over which the theory can be successfully applied, improving the accuracy of measurements made on thin samples, i.e., less than a few hundred microns. Proper coaxial alignment of all optics in the system is also important, as appreciable angular or lateral offsets from the central axis will start to introduce systematic errors that cause inaccuracy in the measured Δz. Whilst parabolic mirrors can be awkward to set up and are not available in as many different focal lengths as lenses, they do offer an inexpensive and reliable solution for most samples. It would be necessary to apply NA correction for either lens or mirror configurations above an NA of approximately 0.18.

Funding. Engineering and Physical Sciences Research Council (EPSRC) (EP/M010473/1).

Acknowledgment. We dedicate this work to our colleague Dr. Helen D. Ford (1963—2018). The underlying data can be accessed through the Cranfield University data repository at 10.17862/cranfield.rd.7993745.

REFERENCES

1. B. L. Danielson and C. Y. Boisrobert, "Absolute optical ranging using low coherence interferometry," Appl. Opt. **30**, 2975–2979 (1991).
2. D. Huang, E. A. Swanson, C. P. Lin, J. S. Schuman, W. G. Stinson, W. Chang, M. R. Hee, T. Flotte, K. Gregory, C. A. Puliafito, and J. G. Fujimoto, "Optical coherence tomography," Science **254**, 1178–1181 (1991).
3. W. V. Sorin and D. F. Gray, "Simultaneous thickness and group index measurement using optical low-coherence reflectometry," IEEE Photon. Technol. Lett. **4**, 105–107 (1992).
4. G. J. Tearney, M. E. Brezinsky, J. F. Southern, B. E. Bouma, M. R. Hee, and J. G. Fujimoto, "Determination of the refractive index of highly scattering human tissue by optical coherence tomography," Opt. Lett. **20**, 2258–2260 (1995).
5. T. Fukano and I. Yamaguchi, "Simultaneous measurement of thickness and refractive indices of multiple layers by a low-coherence confocal interference microscope," Opt. Lett. **21**, 1942–1944 (1996).

6. M. Haruna, M. Ohmi, T. Misuyama, H. Tajiri, H. Maruyama, and M. Hashimoto, "Simultaneous measurement of the phase and group indices and the thickness of transparent plates by low-coherence interferometry," Opt. Lett. **23**, 966–968 (1998).
7. H. Maruyama, T. Mitsuyama, M. Ohmi, and M. Haruna, "Simultaneous measurement of refractive index and thickness by low coherence interferometry considering chromatic dispersion of index," Opt. Rev. **7**, 468–472 (2000).
8. M. Ohmi, H. Nishi, Y. Konisha, Y. Yamada, and M. Haruna, "High-speed simultaneous measurement of refractive index and thickness of transparent plates by low-coherence interferometry and confocal optics," Meas. Sci. Technol. **15**, 1531–1535 (2004).
9. S. Kim, J. Na, M. J. Kim, and B. H. Lee, "Simultaneous measurement of refractive index and thickness by combining low coherence interferometry and confocal optics," Opt. Express **16**, 5516–5526 (2008).
10. D. Francis, H. D. Ford, and R. P. Tatam, "Spectrometer based refractive index and dispersion measurement using low-coherence interferometry with confocal scanning," Opt. Express **26**, 3604–3617 (2018).
11. C. J. R. Sheppard, "Aberrations in high aperture conventional and confocal imaging systems," Appl. Opt. **27**, 4782–4786 (1988).
12. S. Hell, G. Reiner, C. Cremer, and E. H. K. Stelzer, "Aberrations in confocal fluorescence microscopy induced by mismatches in refractive index," J. Microsc. **169**, 391–405 (1993).
13. J. J. Stamnes and D. Velauthapillai, "Focal shifts through a plane interface," Opt. Commun. **282**, 2286–2291 (2009).
14. C. J. R. Sheppard and P. Török, "Effects of specimen refractive index on confocal imaging," J. Microsc. **185**, 366–374 (1997).
15. A. Diasporo, F. Federici, and M. Robello, "Influence of refractive-index mismatch in high-resolution three-dimensional confocal microscopy," Appl. Opt. **41**, 685–690 (2002).
16. D. Iwaniuk, P. Rastogi, and E. Hack, "Correcting spherical aberrations induced by an unknown medium through determination of its refractive index and thickness," Opt. Express **19**, 19407–19414 (2011).
17. K. Newman, "An introduction to off-axis parabolic mirrors," 2013, https://wp.optics.arizona.edu/optomech/wpcontent/uploads/sites/53/2016/10/521_Tutorial_Newman_Kevin.PDF.
18. T. G. van Leeuwen, D. J. Faber, and M. C. Aalders, "Measurement of the axial point spread function in scattering media using single-mode fiber-based optical coherence tomography," IEEE J. Sel. Top. Quantum **9**, 227–233 (2003).
19. Y. X. Yuan, "A review of trust region algorithms for optimization," ICIAM **99**, 271–282 (2011).
20. K. Larkin, "Efficient nonlinear algorithm for envelope detection in white light interferometry," J. Opt. Soc. Am. A **13**, 832–843 (1996).
21. P. Liu, R. M. Groves, and R. Benedictus, "Signal processing in optical coherence tomography for aerospace material characterization," Opt. Eng. **52**, 032201 (2013).
22. M. N. Polyanskiy, "Refractive index database," 2019, https://refractiveindex.info.

Influence of aberrations on confocal-based remote refractive index measureme

Ford, Helen D.

2019-08-13

Ford HD, Francis D, Hallam JM, Tatam RP. (2019) Influence of aberrations on confocal-based remote refractive index measurements. Applied Optics, Volume 58, Issue 24, August 2019, pp. 6474-6485
https://doi.org/10.1364/AO.58.006474